Available online at www.sciencedirect.com
ScienceDirect
Trans. Nonferrous Met. Soc. China 35(2025) 3093−3107
Transactions of Nonferrous Metals Society of China
www.tnmsc.cn

Preparation, electrochemical properties and energy storage mechanism of vanadium-based Prussian blue analogues as cathode materials for aqueous ammonium ion batteries

Tao-tao LI[1], Jin-peng QU[1], Lu-lu ZHAO[1], Peng-fei WANG[1], Jun-hong ZHANG[2], Ting-feng YI[1,3]

1. School of Materials Science and Engineering, Northeastern University, Shenyang 110819, China;
2. Shandong Provincial Key Laboratory of Chemical Energy Storage and Novel Cell Technology, College of Chemistry and Chemical Engineering, Liaocheng University, Liaocheng 252059, China;
3. Key Laboratory of Dielectric and Electrolyte Functional Materials of Hebei Province, School of Resources and Materials, Northeastern University at Qinhuangdao, Qinhuangdao 066004, China

Received 13 January 2024; accepted 20 September 2024

Abstract: To explore high-performance cathode materials for aqueous ammonium ion batteries (AAIBs), vanadium-based Prussian blue analogue composites (VFe-PBAs) were prepared by hydrothermal coprecipitation method to enhance the reversible storage of NH_4^+. Benefiting from the stable three-dimensional structure and spacious gap position, VFe-PBAs-2 cathode displays excellent electrochemical activity and rate performance, achieving a high specific capacity of 84.3 mA·h/g at a current density of 1000 mA/g. In addition, VFe-PBAs-2 cathode also shows impressive long-term cycle durability with 85.2% capacity retention after 3×10^4 cycles at 5000 mA/g. The synthesized cathode materials combined with the high electrochemical activity of vanadium ions significantly promote the rapid transfer of NH_4^+. Furthermore, NH_4^+ embedding/extraction mechanism of VFe-PBAs-2 cathode was revealed by electrochemical kinetics tests and advanced ex-situ characterizations. The experimental results demonstrate that vanadium-modified VFe-PBAs-2 as a cathode material can remarkably improve the capacity, electrochemical activity and cycling stability of AAIBs to achieve high performance NH_4^+ storage.

Key words: energy storage; aqueous ammonium ion battery; Prussian blue analogues; rate performance; cycling stability

1 Introduction

Considering the growing environmental pollution and energy crisis associated with the burning of fossil fuels, the development and search for sustainable and clean energy sources are the main trends to solve these problems. Despite the huge commercial success of rechargeable lithium ion batteries (LIBs), the flammability of organic electrolytes used in LIBs may cause safety problems, thus hindering their further application in grid-scale energy storage [1,2]. The advanced electrochemical energy conversion and storage systems should have the advantages of being easy to prepare, environmentally friendly, and highly efficient. Rechargeable batteries based on aqueous electrolytes have garnered significant interest due to their inherent safety, cost-effectiveness, and environmental friendliness. They are considered as promising devices to effectively integrate clean energy sources such as solar and wind with smart technologies [3−5].

Significant efforts have been devoted to the

Corresponding author: Jun-hong ZHANG, E-mail: zhangjunhong@lcu.edu.cn;
Ting-feng YI, Tel: +86-13933906579, E-mail: tfyihit@163.com
https://doi.org/10.1016/S1003-6326(25)66868-3

development of aqueous batteries utilizing metallic ions such as Li^+, Na^+, Zn^{2+}, Mg^{2+}, and Al^{3+} as charge carriers [6−9]. In contrast to these metal ions, non-metallic NH_4^+ serves as a charge carrier with abundant synthetic resources, relatively small hydrated ion size (3.31 Å), low molar mass (18 g/mol), and fast diffusion kinetics. The tetrahedral structure of NH_4^+ exhibits unique intercalation behavior due to the formation and breakage of hydrogen bonds, which contributes to achieving excellent electrochemical performance [10,11]. In aqueous ammonium ion batteries (AAIBs) systems, Prussium blue analogue composites (PBAs) are widely used as electrode materials for energy storage of alkali metal ions owing to their large open framework and abundant ionic insertion sites [12,13]. The synthesis of PBAs does not require a high-temperature calcination process or expensive precursors, which can reduce the manufacturing cost of PBAs to some extent [14−17]. Generally, PBAs can be obtained by co-precipitation, electrochemical deposition, ball milling, etc. Among them, the simple co-precipitation method is widely used to prepare host PBAs for AAIBs, with the potential for large-scale applications. The representative formula for PBAs is $A_xL_y[M(CN)_6]_{z-n}\cdot H_2O$, where A represents alkali metal ions or NH_4^+, and L and M typically represent transition metal ions [18,19]. Rational element substitution can significantly improve the electrochemical properties of PBAs. Some substitution elements can act as pillars in the framework, preventing the lattice strain and suppressing large volume changes, thereby greatly improving structural stability. The lattice properties and redox behaviors can be modified by replacing the N-coordinating metal with one or more other elements [20,21]. YANG et al [22] reported an aqueous rechargeable copper−ammonium hybrid battery (N-CuHCF) with an operating mechanism consisting of a reversible NH_4^+ insertion/extraction reaction at the cathode and a copper plating/stripping reaction at the anode. The unique operating mechanism offered a long cycle life (more than 1×10^4 cycles). Even with a high mass of N-CuHCF at the cathode (0.2 A/g), the N-CuHCF exhibited high specific capacity and long-life characteristics (1000 cycles) with a capacity retention of 65%. FAN et al [23] prepared a series of $Cu_xNi_{2-x}Fe(CN)_6$ cathodes for AIBs. The copper content in nickel hexacyanoferrate increased the reaction potential and capacity. The $Cu_{0.4}Ni_{1.6}$-$Fe(CN)_6$ cathode exhibited the best cycling performance (97.54% capacity retention at 0.3*C*) and the highest rate capacity (41.4 mA·h/g at 10*C*).

In this study, vanadium-based PBAs (VFe-PBAs) materials were prepared by a simple hydrothermal co-precipitation method. The energy storage mechanism of VFe-PBAs-2 in AAIBs was further investigated by ex-situ XRD and ex-situ XPS measurements. Active sites of V^{4+}/V^{5+}, Fe^{2+}/Fe^{3+}, and structural stability promote the efficient electrochemical properties of VFe-PBAs-2. The conversion of the V and Fe elements between different valence states not only provides abundant redox reaction paths but also optimizes the internal electrochemical environment so that AAIBs can maintain high stability and efficiency during charging and discharging processes. Therefore, VFe-PBAs-2 as a cathode material exhibits excellent long-term cycling stability in AAIBs, retaining both 85.2% of its high specific capacity after 3×10^4 cycles at 5000 mA/g and superior rate capacity. This work provides a new strategy for preparing high-performance cathodes by using PBAs materials.

2 Experimental

2.1 Materials and chemicals

All chemicals were used without further purification. Ammonium metavanadate (NH_4VO_3, ≥99.0%), potassium ferricyanide ($K_3[Fe(CN)_6]$, ≥98.0%), oxalic acid ($H_2C_2O_4$, ≥98.0%), and ammonium sulfate ($(NH_4)_2SO_4$, ≥98.0%) were purchased from Aladdin Reagent Co., Ltd. (Shanghai, China). Ethanol, polytetrafluoroethylene (PTFE) and carbon paper were purchased from Sinopharm Chemical Reagent Co., Ltd. (Shanghai, China).

2.2 Material preparation

Synthesis of VFe-PBAs-2: The VFe-PBAs-2 materials with the lamellar cubic structure were synthesized by hydrothermal co-precipitation method. Briefly, 4 mmol of NH_4VO_3 and 4 mmol of $K_3[Fe(CN)_6]$ were mixed with 70 mL of ultrapure water. Then, 10 mmol of anhydrous oxalic acid was added and the mixture was stirred uniformly for 30 min. The mixture was transferred to a 100 mL

Teflon-lined stainless-steel autoclave, followed by hydrothermal treatment at 180 °C for 8 h. After natural cooling, the resulting products were centrifuged several times with deionized water and ethanol, and then dried under vacuum at 60 °C overnight. The final powder products were named VFe-PBAs-2.

Synthesis of VFe-PBAs-1: The procedure was the same as that for VFe-PBAS-2 except that 2 mmol of NH_4VO_3 is used, while all other reaction parameters remain unchanged.

Synthesis of VFe-PBAs-3: The procedure was the same as that for VFe-PBAs-2 except that 8 mmol of NH_4VO_3 is used, while all other reaction parameters remain unchanged.

2.3 Material characterization

Scanning electron microscopy measurement (SEM) was carried out with a Super 55 field emission scanning electron microscope. Transmission electron microscopy (TEM) images were collected using a Talos F200X transmission electron microscope. The crystal structure was determined by X-ray diffraction (XRD, Rigaku Smarlab) with a 2D detector (Cu K_α radiation, λ=1.5418 Å) in a continuous scan mode at a speed of 5 (°)/min. The elemental species and valence states within the material were identified by X-ray photoelectron spectroscopy (XPS, ESCALAB 250Xi). Raman spectra of the samples were obtained on a Micro-Raman spectrometer (LABRAM-HR confocal laser) using an argon laser with a wavelength of 514.5 nm. Fourier transform infrared (FT-IR) spectra were recorded on a Thermo Fisher Nicolet 6700 FT-IR spectrometer. Thermogravimetric analysis (TGA) was performed using an SDT Q600. An inductively coupled plasma emission spectrometer (ICP-OES, Thermo ICAP PRO) was used.

2.4 Electrochemical measurements

A homogeneous slurry containing the active substance, acetylene black and PTFE (taken in a mass ratio of 7∶2∶1) and an appropriate amount of anhydrous ethanol was coated on 1 cm × 1.5 cm carbon paper. The electrode area was 1.5 cm^2. The mass loading of the active substance on the electrode was around 2.5 mg/cm^2, and the thickness of the working electrode was about 30 μm. Then, vacuum drying was carried out at 80 °C for 12 h to form a working electrode. The electrochemical performance of VFe-PBAs electrodes was examined in a three-electrode system consisting of a working electrode (active material), a counter electrode (Pt sheet), and a reference electrode (saturated calomel electrode (SCE, φ=0.244 V (vs standard hydrogen electrode, SHE)). The electrolyte of the VFe-PBAs electrode was the homogeneous solution of 1.0 mol/L $(NH_4)_2SO_4$ solution. Cyclic voltammetry (CV) measurements were carried out on the CHI602E electrochemical workstation (Chenhua Instrument, Shanghai, China). The galvanostatic charge−discharge (GCD) performance test was conducted in the same voltage range on the Neware (Shenzhen, China). Electrochemical impedance spectroscopy (EIS) test was performed on a Zahner electrochemical workstation (Germany) with a frequency from 100 kHz to 0.01 Hz.

3 Results and discussion

3.1 Microstructure and composition of VFe-PBAs materials

The morphology of VFe-PBAs can be investigated through SEM and TEM tests. SEM images of all samples display cubic structures with relatively uniform size (Figs. 1(a−f)), indicating that they have inherited a stable three-dimensional framework of PBAs. Interestingly, VFe-PBAs-2 exhibits the best cubic morphology distribution compared to VFe-PBAs-1 and VFe-PBAs-3, suggesting that the proportion of precursors could effectively optimize the microstructure of the sample [24−26]. TEM was utilized to further observe the morphology of VFe-PBAs-2 (Figs. 1(g) and (h)), and VFe-PBAs-2 is composed of multiple lamellae stacked vertically and horizontally to form a cube. The distinct layered structure significantly increases the specific surface area of the material, providing a larger electrolyte−electrode interface for NH_4^+ storage and allowing rapid charge transfer and ion diffusion. High-resolution TEM image shows no obvious lattice fringes and diffraction spots, which may be related to the density and thickness of the samples (Fig. 1(i)). Energy dispersive spectroscopy (EDS) mappings prove the homogeneous distribution of V, Fe, N, and C elements throughout the cube of VFe-PBAs-2 (Fig. 1(j)).

The crystal structures of VFe-PBAs-1, VFe-PBAs-2, and VFe-PBAs-3 were determined by

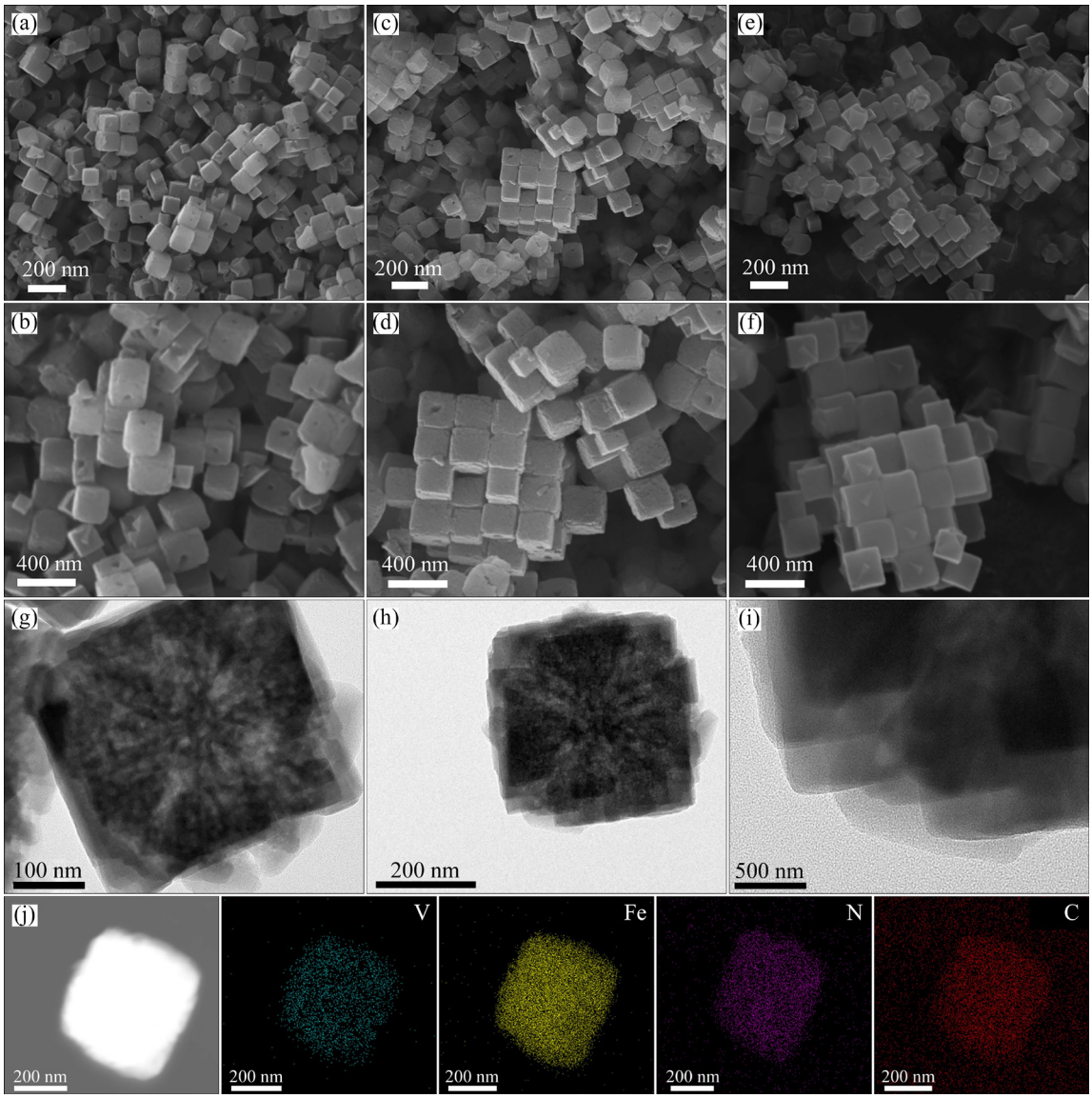

Fig. 1 SEM images of VFe-PBAs-1 (a, b), VFe-PBAs-2 (c, d), and VFe-PBAs-3 (e, f); TEM images (g, h), high-resolution TEM image (i), and corresponding EDS mappings (j) of VFe-PBAs-2

XRD analysis. As shown in Fig. 2(a), the positions of the characteristic diffraction peaks of all samples are in general agreement with the standard card of JCPDS No. 42-1440 [13,27], indicating that the fabricated materials are pure and well crystallized. All XRD peaks exhibit their typical face-centered cubic (FCC) structure with the space group of $Fm\bar{3}m$ and the same (200), (220), (400), (420), (422), (440), (600), and (620) crystal planes without any additional diffraction peaks. The results demonstrate that all the synthesized VFe-PBA materials are high-purity and free from impurities. The lattice constants (a=b=c) of the prepared samples are 10.14 Å (VFe-PBAs-1), 10.18 Å (VFe-PBAs-2), and 10.10 Å (VFe-PBAs-3), which can be calculated from the XRD results. The lattice constants of the samples are slightly different from the standard cards, indicating that their crystals may contain different amounts of K^+ inside to occupy the lattice sites of the VFe-PBAs cathode materials [13,28].

The FT-IR spectra show the unique chemical bonding of the VFe-PBAs materials (Fig. 2(b)). The absorption from 550 to 650 cm^{-1} corresponds to the stretching vibrations of Fe—CN. The peaks located at 2098 and 968 cm^{-1} can be attributed to the vibrations of —C≡N and V═O bonds, respectively [29−31]. It is worth noting that the stretching vibration peak of O—H at 3425 cm^{-1} and the bending vibration peak of H—O—H at

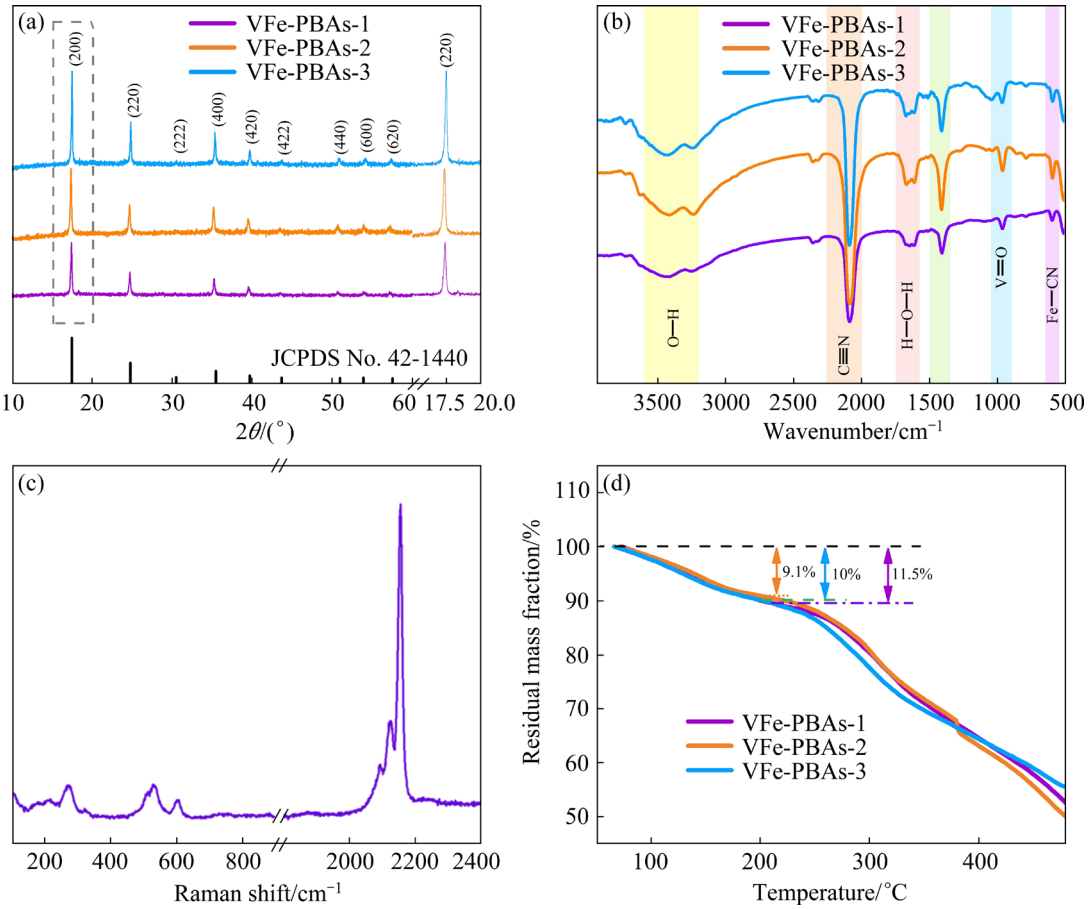

Fig. 2 XRD patterns (a), FT-IR spectra (b) and TGA curves (d) of different VB-PBAs, and Raman spectrum of VFe-PBAs-2 (c)

1625 cm^{-1} demonstrate the existence of interstitial water in the VFe-PBAs lattice [32]. The bonding structure of the VFe-PBAs-2 sample was further confirmed by Raman spectrum (Fig. 2(c)). The characteristic peaks between 150 and 350 cm^{-1} are associated with the deformation vibrations of C—Fe—C and Fe—C≡N—V. The stretching vibrations of the Fe—C bond can be assigned to 533.7 and 600 cm^{-1}. The peaks at 2050−2250 cm^{-1} are ascribed to the vibrations of the —C≡N functional group associated with Fe ions in different oxidation states [33]. TGA and ICP-OES were applied to assessing the absorbed and crystalline water content of VFe-PBAs. The significant mass losses of 11.5%, 9.1%, and 10% for VFe-PBAs-1, VFe-PBAs-2, and VFe-PBAs-3, respectively at ~200 °C can be attributed to the removal of crystalline and absorbed water, respectively (Fig. 2(d)) [13,33]. Based on the results obtained from TGA and ICP-OES, we can deduce the chemical formula of the synthesized sample as follows: $K_{0.24}V_{0.38}[Fe(CN)_6]\cdot 1.74H_2O$ for VFe-PBAs-1, $K_{0.22}V_{0.46}[Fe(CN)_6]\cdot 1.36H_2O$ for VFe-PBAs-2, and $K_{0.21}V_{0.67}[Fe(CN)_6]\cdot 1.6H_2O$ for VFe-PBAs-3 (Table 1).

Table 1 ICP-OES test data of VFe-PBAs materials

Material	Content/wt.%		
	K	V	Fe
VFe-PBAs-1	3.4	7.1	20.6
VFe-PBAs-2	3.2	8.7	20.9
VFe-PBAs-3	2.9	12	19.8

XPS was used to determine the elemental composition and surface chemical state of the VFe-PBAs. Figure 3(a) confirms the presence of elements Fe, O, V, C, and N. The high-resolution O 1s spectrum reveals the presence of multiple chemical states of oxygen in the sample, and the peaks located at 529.7, 531.1, and 532.7 eV correspond to O^{2-} in V═O, crystal H_2O, and adsorbed H_2O from the environment, respectively (Fig. 3(b)) [34−36]. The Fe 2p spectrum exhibits

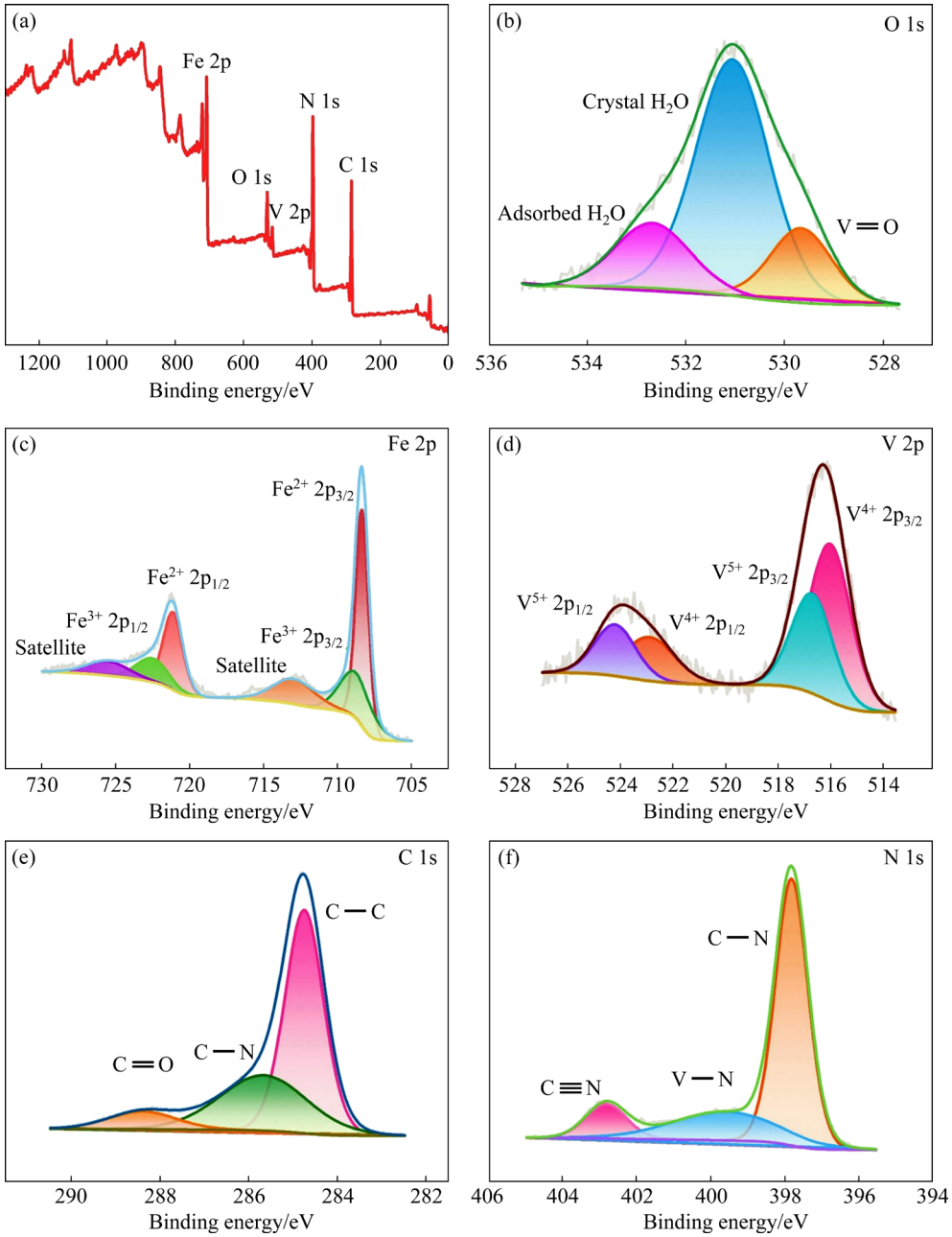

Fig. 3 XPS survey spectrum (a) and corresponding high-resolution XPS spectra (b−e) of VB-PBAs-2

two peaks of Fe^{2+} (721.2 eV for Fe^{2+} $2p_{1/2}$ and 708.3 eV for Fe^{2+} $2p_{3/2}$), and Fe^{3+} (722.6 eV for Fe^{3+} $2p_{1/2}$ and 709.0 eV for Fe^{3+} $2p_{3/2}$). Besides, there are two satellite peaks at 725.61 and 713.4 eV belonging to Fe $2p_{1/2}$ and Fe $2p_{3/2}$, respectively (Fig. 3(c)) [33,37]. For the V 2p spectrum, the peaks of both V $2p_{3/2}$ and V $2p_{1/2}$ can be assigned to V^{5+} (516.7 and 524.2 eV) and V^{4+} (522.8 and 516.1 eV), respectively (Fig. 3(d)). It can be confirmed that the prepared VFe-PBAs-2 contains both V^{5+} and V^{4+} [38]. The C 1s spectrum displays the presence of C—C (284.7 eV), C—N (285.6 eV), and O—C═O (288.4 eV) (Fig. 3(e)) [39]. The N 1s spectrum is deconvoluted into three peaks centered at 397.8, 399.6, and 402.8 eV, which can be attributed to C—N, V—N, and —C≡N bonds in $[Fe(CN)_6]^{4-}$, respectively (Fig. 3(f)) [13]. The molar fraction of the elements is shown in Table 2. The Fe/N molar ratio demonstrates that Fe is present not only in $[Fe(CN)_6]^{4-}$ but also in other forms, such as coupling with V [23,26]. Some oxygen elements combine with vanadium to form VO^{2+}; some of VO^{2+} is generated from water introduced during hydrothermal reactions [39]. From the above results, it can be concluded that the VFe-PBAs materials have been successfully fabricated.

Table 2 Contents of elements (C, N, O, V, Fe) in VFe-PBAs measured by XPS

Element	Content/at.%
C 1s	44.58
N 1s	33.51
O 1s	10.10
V 2p	2.70
Fe 2p	8.01
K 2p	1.21

3.2 Electrochemical performance of VFe-PBAs as cathodes

Subsequently, the electrochemical performance of VFe-PBAs as cathodes in AAIBs was detailly investigated. Figure 4(a) displays the CV curves of the three cathodes at a scan rate of 0.1 mV/s. All the VFe-PBAs cathode materials have similar curves with a pair of distinct oxidation and reduction peaks at around 0.23 and 0.185 V (vs SCE), as well as a pair of redox peaks with insignificant peaks between 0.7 and 1 V (vs SCE). Among them,

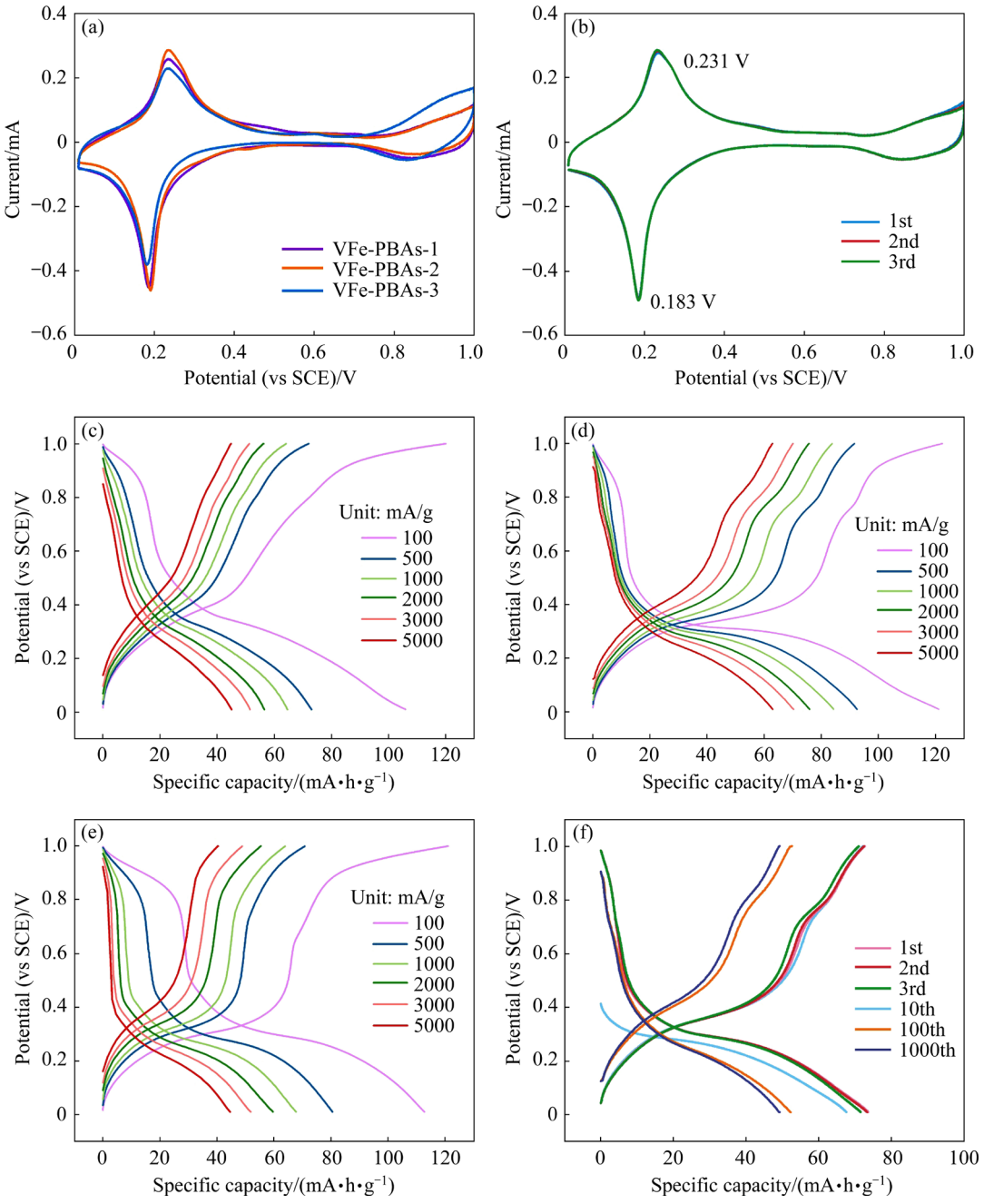

Fig. 4 (a) CV curves of VFe-PBAs; (b) CV curves of VFe-PBAs-2 of initial three cycles at 1.0 mV/s; (c−e) GCD curves of VFe-PBAs-1, VFe-PBAs-2 and VFe-PBAs-3 at various current densities from 100 to 5000 mA·h/g, respectively; (f) GCD curves of VFe-PBAs-2 at 5000 mA/g and different cycles

VFe-PBAs-2 shows the smallest potential difference between the oxidation and reduction peaks, which is favorable for the reversible insertion and extraction of NH_4^+ and smaller polarization. It is important to mention that the CV curves of the first three cycles of VFe-PBAs-2 perfectly overlap (Fig. 4(b)), indicating that VFe-PBAs-2 has excellent structural reversibility. The reduction and oxidation processes at 0.183 and 0.231 V (vs SCE) correspond to the Fe^{2+}/Fe^{3+} and V^{4+}/V^{5+} redox processes, respectively. According to previous reports [32,40], the reduction and oxidation peaks are assumed to be related to the reversible electrochemical reactions of Fe(II)$\rightleftharpoons$Fe(III)+e, and $[V(IV)O_2H]^+ \rightleftharpoons [V(V)O_2]^+ + H^+ + e$, respectively. Several redox processes occur in the VFe-PBA-2 cathode, facilitating electron storage processes [40,41]. Figures 4(c−e) present the GCD curves of VFe-PBAs-1, VFe-PBAs-2, and VFe-PBAs-3 at different current densities from 100 to 5000 mA/g, respectively. It can be observed that the trend of charge−discharge curves is similar, and the charge−discharge platform at around 0.3 V (vs SCE) gradually shrinks with increasing current density. The initial galvanostatic charge−discharge specific capacities of the three electrode materials at 100 mA/g are 105.8/120 mA·h/g, 121.2/122.4 mA·h/g, and 112.7/120.9 mA·h/g, respectively, with the corresponding coulombic efficiencies of 87.9%, 99.0%, and 93.2%. VFe-PBAs-2 exhibits a pair of more pronounced potential plateaus, along with higher capacity and coulombic efficiency, in comparison to the other two cathodes. This implies that VFe-PBAs-2 possesses a more stable framework structure. Figure 4(f) shows the cycling behavior of VFe-PBAs-2 at 5000 mA/g. The GCD curves of the first three cycles almost completely overlap. The specific capacity of VFe-PBAs-2 decreases only slightly in the 100th and 1000th cycles, reflecting good cycling stability and excellent structural stability.

To further demonstrate the advantageous properties of VFe-PBAs-2 as a cathode, the rate performance of VFe-PBAs was tested at different current densities from 100 to 5000 mA/g, as shown in Fig. 5(a). It is clear that VFe-PBAs-2 exhibits the highest specific capacity at each current density, with reversible discharge/charge specific capacities at 100, 500, 1000, 2000, 3000, and 5000 mA/g being 121.1/122.4, 92.5/91.5, 84.3/83.8, 75.8/75.6, 70.3/70.1, and 63.0/62.9 mA·h/g, respectively. During the current density recovery from 5000 to 100 mA/g, the discharge capacity remains at 102.5 mA·h/g without significant reduction. At a current density of 100 mA/g, the charge specific capacity exceeds the discharge specific capacity and exhibits a decreasing trend over 10 cycles. The phenomenon can be attributed to the insufficient time available for the $VO^{2+} \rightleftharpoons VO_2^+$ reaction, leading to the significant loss of vanadium ions. At high current densities, the trend remains stable without any observable capacity drop, and the discharge−charge specific capacities of the samples remain constant, demonstrating their excellent ammoniation/de-ammoniation performance. As shown in Fig. 5(b), the VFe-PBAs electrodes show superior cycling performance at 5000 mA/g. The discharge capacities of the VFe-PBAs-1, VFe-PBAs-2, and VFe-PBAs-3 electrodes are 46.4, 59.2, and 40.1 mA·h/g, respectively, with capacity retention rates of 84%, 98.2%, and 91.5% after 5000 cycles. VFe-PBAs-2 displays not only the best specific capacity but also the best capacity retention. This can be attributed to its more stable lattice structure and sufficiently large pore space, which facilitate rapid kinetics of NH_4^+. The cycling performance curves occasionally fluctuate due to environmental factors that affect the diffusion and transport rates of NH_4^+. The VFe-PBAs-2 cathode also exhibits remarkable long-term cycling performance at a high current density of 5000 mA/g (Fig. 5(c)). It can maintain a discharge capacity of 51.3 mA·h/g with a capacity retention rate of 85.2% (the initial capacity is 60.6 mA·h/g) after 3×10^4 cycles. Additionally, the coulombic efficiency of the cathode can remain at 100% after the initial cycles. The loss of capacity is almost negligible when evenly distributed over each cycle. These results show that VFe-PBAs-2 material has good capacity retention and outstanding coulombic efficiency after repeated cycling, demonstrating the structural stability and the potential for the practical application.

In order to assess the reaction kinetics of the VFe-PBAs cathodes in AAIBs, CV measurements were conducted at different scan rates (Figs. 6(a−c)). The CV curves of all samples have similar redox peaks. Increasing the scan rate causes the current

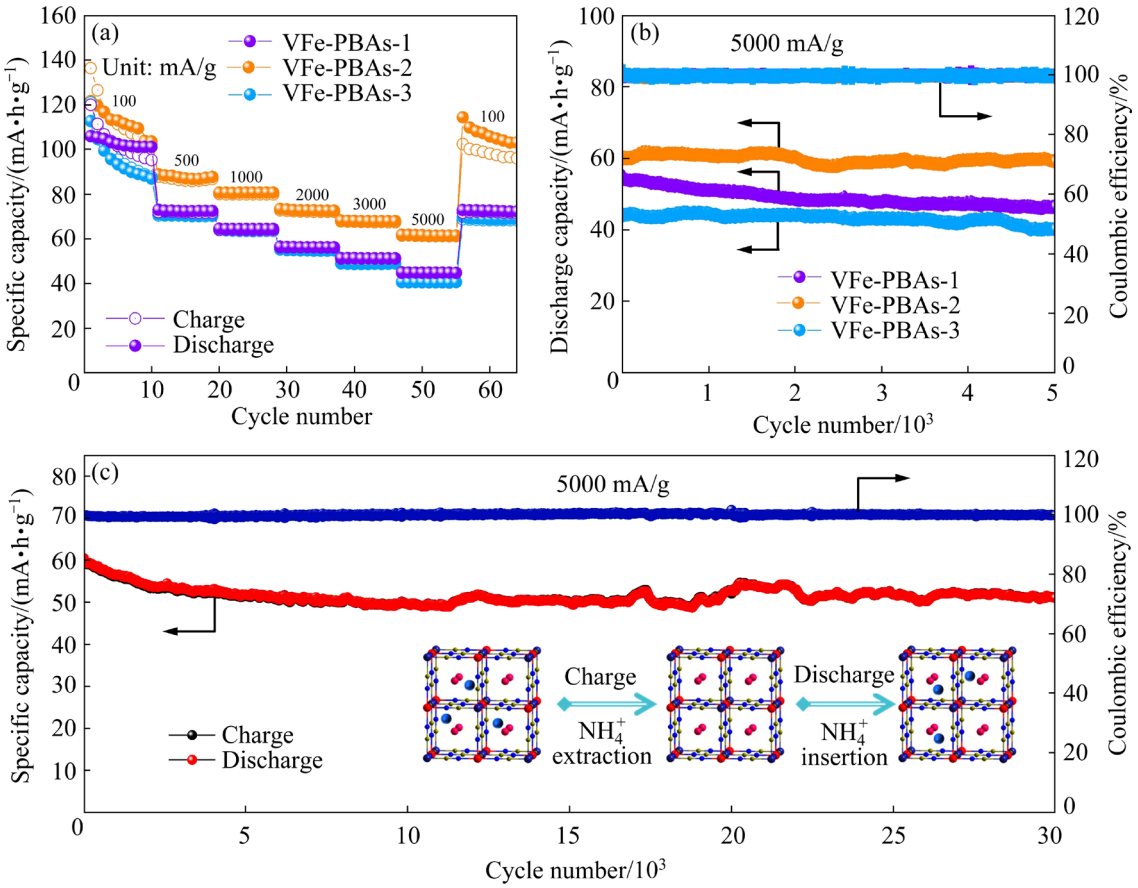

Fig. 5 (a, b) Rate capability and cycling performance of VFe-PBAs, respectively; (c) Long-term cycling capacity of VFe-PBAs-2 at 5000 mA/g (the inset is the schematic illustration of NH_4^+ insertion/extraction into/from VFe-PBAs-2)

region and redox peaks to shift to higher or lower potentials, which is attributed to the effect of internal polarization of the VFe-PBAs cathode. Equations (1) and (2) describe the relationship between peak current (I) and scan rate (v) of the CV curves [42]:

$$I=av^b \tag{1}$$

$$\lg I=b \lg v + \lg a \tag{2}$$

where a and b are constants.

The reaction process is primarily controlled by ion diffusion when the value of b approaches 0.5. On the other hand, when the b value reaches 1, the corresponding electrochemical behavior is primarily governed by capacitance. The b values of Peaks 1 and 2 of the VFe-PBAs-1, VFe-PBAs-2, and VFe-PBAs-3 samples are calculated to be 0.70/0.76, 0.75/0.70, and 0.63/0.68, respectively, by fitting the $\lg I$−$\lg v$ plots of the two peaks (Figs. 6(d−f)). Therefore, the reaction process of the VFe-PBAs is controlled by both pseudocapacitance contribution and Faraday diffusion. Specifically, Faraday diffusion dominates at low current densities, while pseudocapacitance controls at high current densities, thereby contributing to the excellent rate performance and long cycling stability of the VFe-PBAs electrodes. To probe the capacitance contribution to the overall cell system, the pseudocapacitance contribution and the diffusion contribution percentages are calculated as follows [43]:

$$I=k_1v+k_2v^{1/2} \tag{3}$$

$$I/v^{1/2}=k_1v^{1/2}+k_2 \tag{4}$$

where k_1 and k_2 are constants, k_1v is the pseudocapacitance contribution, and $k_2v^{1/2}$ is the diffusion contribution. As shown in Figs. 6(g−i), the pseudocapacitance contribution of all cathodes increases with increasing the scan rate. The pseudocapacitance contributions of VFe-PBAs-2 increase from 54.1% to 84.4% with increasing the scan rate from 0.1 to 2 mV/s, indicating that surface-controlled processes primarily govern the electrochemical reactions.

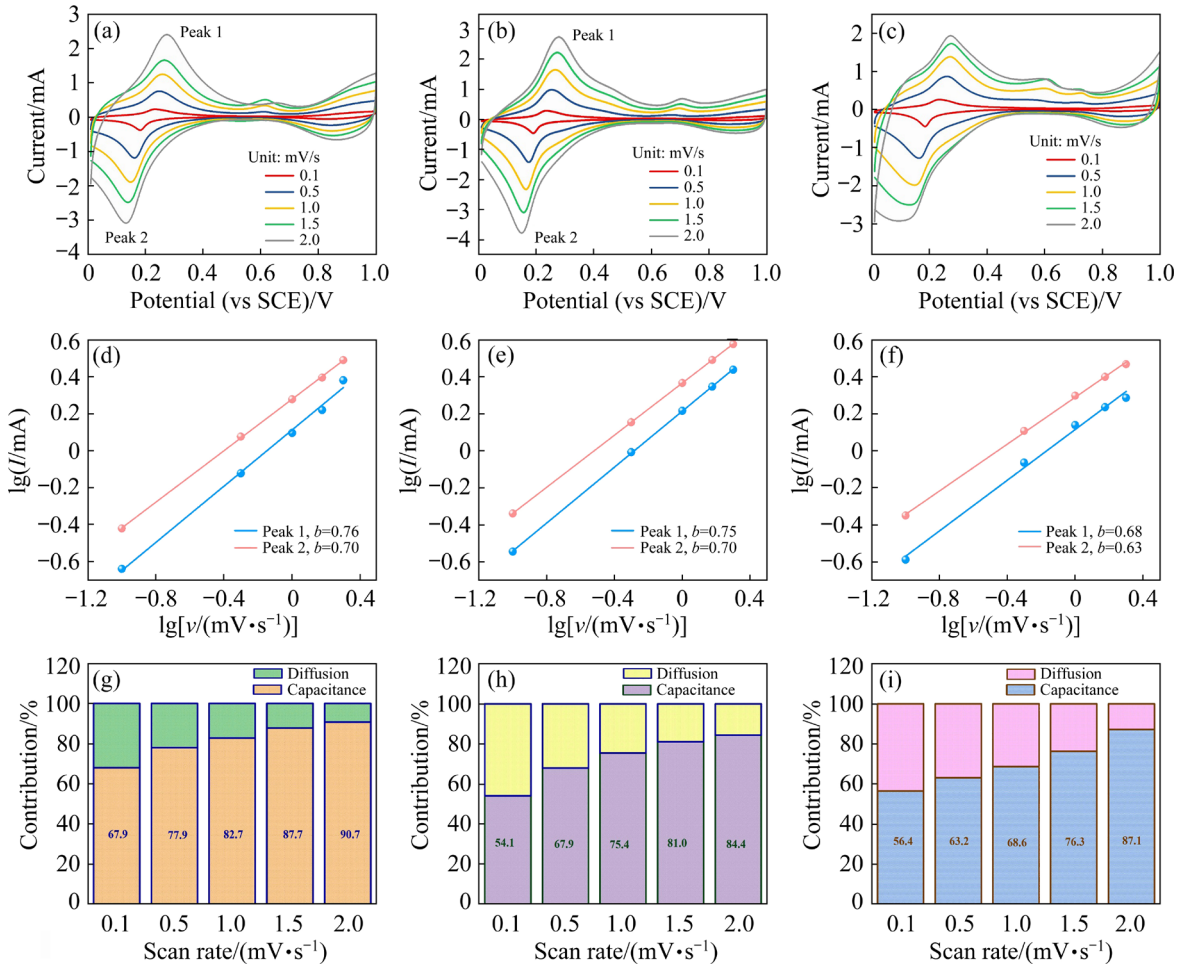

Fig. 6 CV curves of VFe-PBAs-1 (a), VFe-PBAs-2 (b), and VFe-PBAs-3 (c) at different scan rates (0.1−2.0 mV/s); $\lg I - \lg v$ curves of VFe-PBAs-1 (d), VFe-PBAs-2 (e), and VFe-PBAs-3 (f) at specific peak current; Capacity contributions of VFe-PBAs-1 (g), VFe-PBAs-2 (h), and VFe-PBAs-3 (i)

The charge transfer and diffusion kinetics of the VFe-PBAs cathodes are investigated using EIS measurements (Fig. 7(a)). All curves exhibit a diagonal line in the low-frequency region, associated with the Warburg resistance (Z_w), and a semicircle in the high-frequency region, corresponding to the charge transfer impedance (R_{ct}). The intercept of the high frequency region at the real axis attributes to a solution resistance (R_s). Based on the equivalent circuit diagram in Fig. 7(b), the values of R_{ct} of VFe-PBAs-1, VFe-PBAs-2, and VFe-PBAs-3 cathodes are calculated to be 63, 31, and 123 Ω, respectively. VFe-PBAs-2 has the smallest R_{ct} among all the samples, proving that the vanadium element doped with the three-dimensional skeleton in the appropriate proportion to synthesize VFe-PBAs materials is conducive to improving the electrochemical reactivity. The NH_4^+ diffusion coefficient (D) of VFe-PBAs electrode materials can be evaluated using the following equations [43,44]:

$$D=\frac{R^2T^2}{2A^2n^4F^4C^2\sigma^2} \tag{5}$$

$$Z_{re}=R_{ct}+R_s+\sigma\omega^{-1/2} \tag{6}$$

where R is the molar gas constant; T is the thermodynamic temperature; A is the electrode surface area; n is the charge transfer number; F is the Faraday constant; C is the concentration of NH_4^+; σ is the Warburg factor; Z_{re} is the real part of the impedance; ω is the angular frequency. The relationship between Z_{re} and $\omega^{-1/2}$ is fitted in Fig. 7(c). The calculated NH_4^+ diffusion coefficients of the VFe-PBAs-1, VFe-PBAs-2, and VFe-PBAs-3 cathodes are 4.13×10^{-13}, 4.87×10^{-13}, and 3.83×10^{-13} cm^2/s, respectively. VFe-PBAs-2 shows the highest diffusion coefficient, indicating its superior electrochemical NH_4^+ storage capacity.

3.3 Reaction mechanisms of VFe-PBAs as cathodes

As the reaction progresses, NH_4^+ insertion/extraction in VFe-PBAs can cause changes in the electrode structure. The structural evolution of NH_4^+ in VFe-PBAs was investigated by measuring the ex-situ XRD patterns of VFe-PBAs-2 under different charge−discharge processes. As shown in Figs. 8(a) and (b), all XRD patterns remain invariable, and no new peaks are formed, revealing that VFe-PBAs-2 maintains its cubic structure throughout the NH_4^+ insertion/extraction process, corresponding to the quasi-solid solution reaction [27,45]. The amplified diffraction peaks of different crystal planes are shown in Fig. 8(c). During the discharge process, with the NH_4^+ embedding in the VFe-PBAs lattice, the XRD peaks shift to higher angles during NH_4^+ insertion, indicating lattice contractions in VFe-PBAs-2. During the charge process, NH_4^+ departs from the VFe-PBAs-2 lattice, and XRD peaks shift to a low angle and return to their original state, demonstrating lattice expansion [46,47]. It is worth mentioning that the continuous

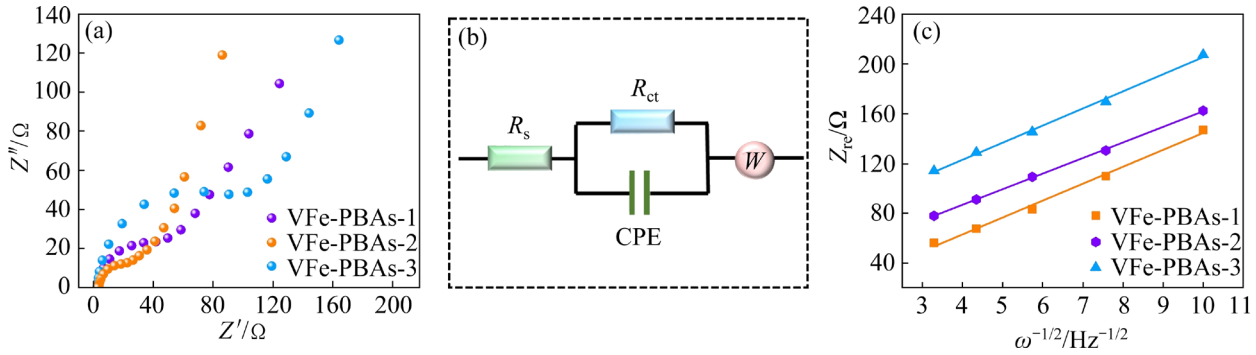

Fig. 7 Nyquist plots (a), equivalent circuit diagram (b), and Z_{re}−$\omega^{-1/2}$ curves (c) of VFe-PBAs materials

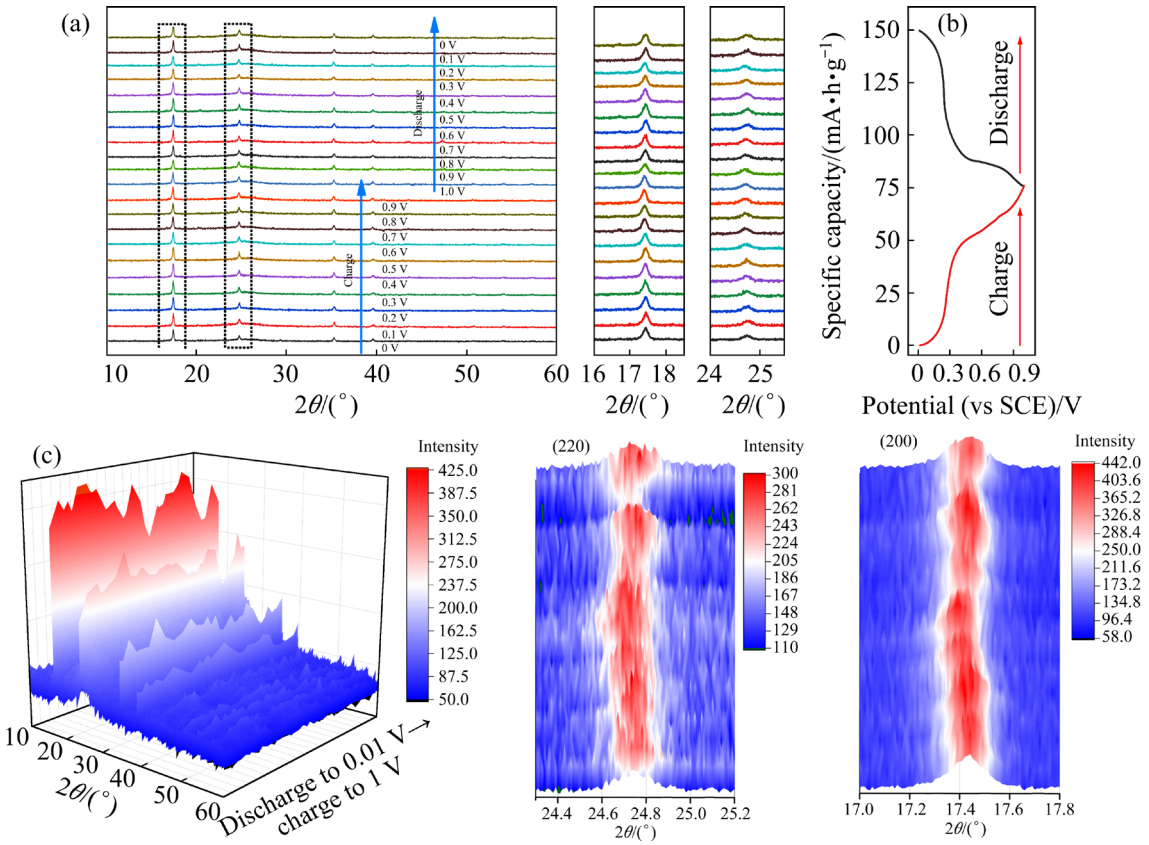

Fig. 8 (a) Ex-situ XRD patterns under charge (from 0 to 1.0 V) and discharge (from 1.0 to 0 V) states and enlarged XRD patterns; (b) Corresponding GCD curve; (c) Contour maps of ex-situ XRD patterns with (200) and (220) crystal planes of VFe-PBAs-2

shift of diffraction peaks indicates the shrinkage and expansion of lattice volume, which is related to the Fe—C bond distance in the VFe-PBAs-2 lattice. Specifically, the lattice contraction that occurs during the discharge process is due to the reduction of Fe^{3+} to Fe^{2+}, leading to the contraction of the Fe — C distance in the lattice framework of VFe-PBAs-2 after the insertion of NH_4^+. During the charge process, the angle returns to the initial state and NH_4^+ is removed from the VFe-PBAs-2 lattice, increasing the Fe—C bond distance and expansion of the VFe-PBA lattice-2 (Fig. 9) [42,48]. The high reversible evolution of the VFe-PBAs-2 structure during charge and discharge processes is the inherent embodiment of excellent cycle performance.

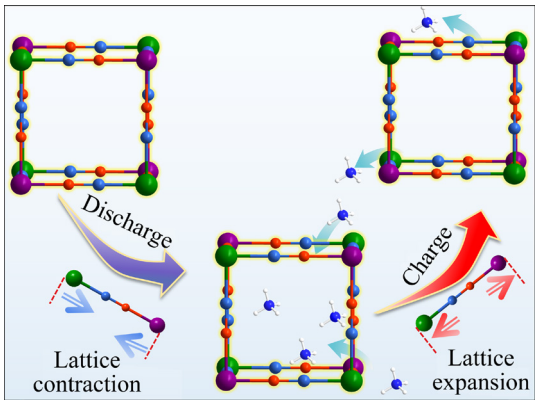

Fig. 9 Schematic illustration of changes in Fe—C bond distance during NH_4^+ insertion/extraction into/from VFe-PBAs-2

To further investigate the electrochemical storage mechanism of VFe-PBAs-2, ex-situ XPS characterization was used to monitor the chemical states of components in VFe-PBAs-2 electrodes at different charge−discharge states. As the discharge progresses (Figs. 10(a−c)), the area of the V^{5+} 2p peak reduces, and the area of the V^{4+} 2p peak increases. The peak of V^{5+} 2p disappears when discharged to 0.01 V (vs SCE), indicating that the V element is involved in electrochemical redox reactions through the (de)insertion of NH_4^+ [49]. Similarly, the area of the Fe^{2+} 2p region decreases while that of the Fe^{3+} 2p region increases during the charge process, demonstrating that Fe^{2+} in the framework is oxidized to Fe^{3+} during the NH_4^+ extraction process (Figs. 10(d−f)); upon further discharging to 0.01 V (vs SCE), the peak intensity ratio of the Fe^{2+}/Fe^{3+} is reversibly enhanced, reflecting the reversibility of the NH_4^+ intercalation process [50,51]. These results prove that the highly reversible redox reaction and stable lattice structure are crucial for the outstanding electrochemical performance of VFe-PBAs-2.

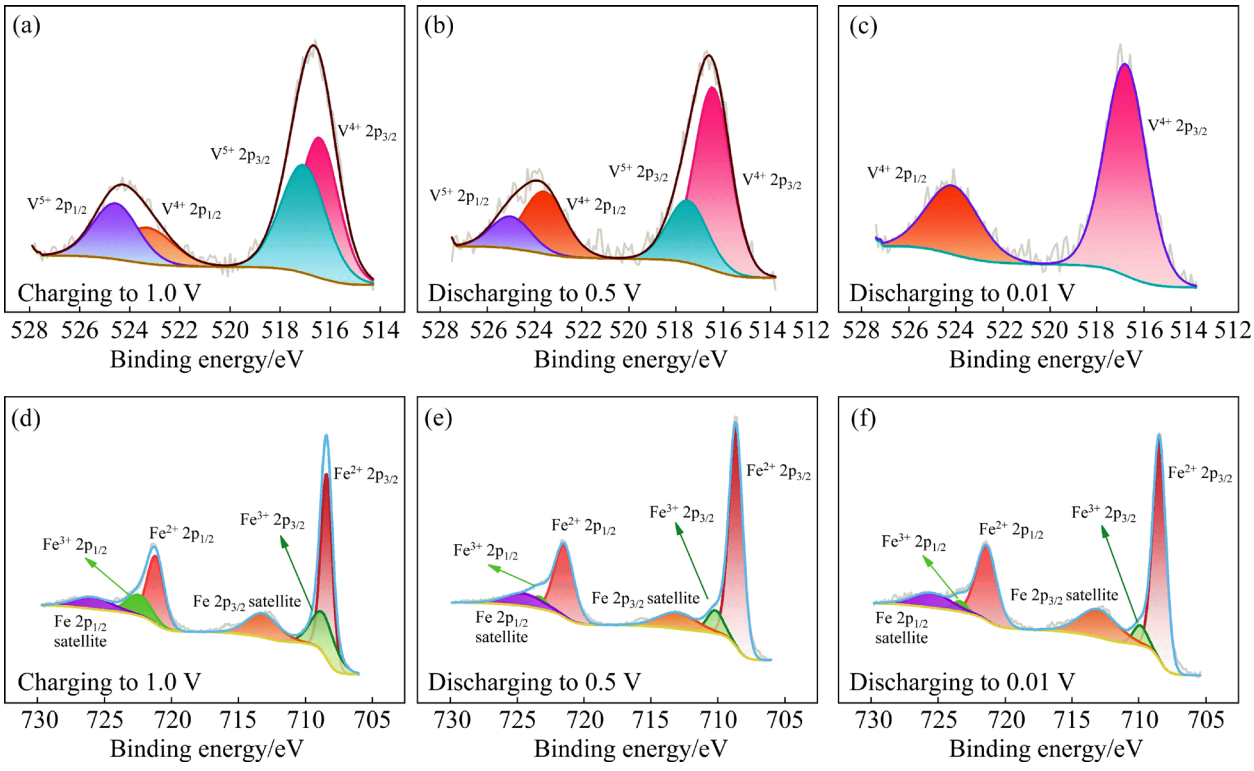

Fig. 10 Ex-situ XPS spectra of V 2p (a−c) and Fe 2p (d−f) for VFe-PBAs-2

4 Conclusions

(1) The vanadium-doped VFe-PBAs cathode materials were prepared by the hydrothermal co-precipitation method and evaluated in AAIBs.

(2) In the experimental screening, VFe-PBAs-2 displays a more prominent electrochemical performance, suggesting that the introduction of appropriate vanadium ions can remarkably increase the capacity, electrochemical kinetics, and cycling stability of batteries.

(3) Specifically, the VFe-PBAs-2 material delivers a superior discharge specific capacity of 121.2 mA·h/g at a current density of 100 mA/g and excellent rate performance with as high as 98.2% capacity retention after 5000 cycles at 5000 mA/g.

(4) The energy storage mechanism of NH_4^+ of the electrode material is validated by electrochemical measurements combined with ex-situ XRD and XPS results. The VFe-PBAs-2 materials exhibit highly reversible structural evolution during the charge and discharge processes, facilitating ion transport and thus enhancing electrochemical activity.

CRediT authorship contribution statement

Tao-tao LI: Data curation, Investigation, Conceptualization, Writing – Original darft; **Jin-peng QU:** Data curation, Investigation; **Lu-lu ZHAO:** Visualization, Writing – Review & editing; **Peng-fei WANG:** Writing – Review & editing; **Jun-hong ZHANG:** Writing – Review & editing, Supervision; **Ting-feng YI:** Investigation, Writing –Review & editing, Supervision, Funding acquisition.

Declaration of competing interest

The authors declare that they have no known competing financial interests or personal relationships that could have appeared to influence the work reported in this paper.

Acknowledgments

This work was supported by the National Natural Science Foundation of China (No. 52374301), the Hebei Provincial Natural Science Foundation, China (No. E2024501010), the Shijiazhuang Basic Research Project, China (No. 241790667A), the Fundamental Research Funds for the Central Universities, China (No. N2423054), and the Performance Subsidy Fund for Key Laboratory of Dielectric and Electrolyte Functional Material of Hebei Province, China (No. 22567627H).

References

[1] WU Fei-xiang, MAIER J, YU Yan. Guidelines and trends for next-generation rechargeable lithium and lithium-ion batteries [J]. Chemical Society Reviews, 2020, 49: 1569−1614.

[2] QIN Mu-lan, YIN Chang-yu, XU Wen, LIU Yang, WEN Jun-hao, SHEN Bin, WANG Wei-gang, LIU Wan-min. Facile synthesis of high capacity P2-type $Na_{2/3}Fe_{1/2}Mn_{1/2}O_2$ cathode material for sodium-ion batteries [J]. Transactions of Nonferrous Metals Society of China, 2021, 31: 2074−2080.

[3] PU Xiang-jun, WANG Hui-ming, ZHAO Dong, YANG Han-xi, AI Xin-ping, CAO Shu-nan, CHEN Zhong-xue, CAO Yu-liang. Recent progress in rechargeable sodium-ion batteries: Toward high-power applications [J]. Small, 2019, 15: e1805427.

[4] WANG De-zhi, LIU Yi-yi, LIU Ruo-qi, GUO Ting, FEI Hao, WU Zhuang-zhi. Preparation and electrocatalytic hydrogen evolution performance of spherical hollow MoS_2/WS_2 heterostructures [J]. Transactions of Nonferrous Metals Society of China, 2023, 33: 1540−1549.

[5] HE Han-bing, LIU Zhen, PENG Chao-qun, LIU Jun, WANG Xiao-feng, ZENG Jing. 3D MoS_2/graphene nanoflowers as anode for advanced lithium-ion batteries [J]. Transactions of Nonferrous Metals Society of China, 2022, 32: 4041−4049.

[6] YANG S H, PARK S K, KANG Y C. MOF-derived $CoSe_2$@N-doped carbon matrix confined in hollow mesoporous carbon nanospheres as high-performance anodes for potassium-ion batteries [J]. Nano-Micro Letters, 2020, 13: 9.

[7] KANG Wen-pei, ZHANG Bing-chen, WANG Zhu-rui, ZHANG Zheng-chun, NIU Mang, AN Xu-guang, MOU Zhen-kai, FAN Xiao-yu, HU Xu-qiang, XI Bao-juan, XIONG Sheng-lin. Synchronous organic−inorganic co-intercalated ammonium vanadate cathode for advanced aqueous zinc-ion batteries [J]. Journal of Energy Chemistry, 2024, 94: 608−617.

[8] HUANG Yu-zhu, XING Lin, PEI Shuang, ZHOU Wei, HU Yu-jie, DENG Wei-na, CHEN Liang, ZHU Hai, CHEN Han. Co_9S_8/CNTs microspheres as superior-performance cathodes in aqueous ammonium-ion batteries [J]. Transactions of Nonferrous Metals Society of China, 2023, 33: 3452−3464.

[9] LIU Zhen, HE Han-bing, LUO Ze-xiang, WANG Xiao-feng, ZENG Jing. 3D printing of customized MnO_2 cathode for aqueous zinc-ion batteries [J]. Transactions of Nonferrous Metals Society of China, 2023, 33: 1193−1204.

[10] XIONG Fang-yu, LIU Xiao-lin, ZUO Chun-li, ZHANG Xiao-lin, YANG Tao, ZHOU Bin-bin, ZHANG Guo-bin, TAN Shuang-shuang, AN Qin-you, CHU P K. Percolating network of anionic vacancies in Prussian blue: Origin of superior ammonium-ion storage performance [J]. The Journal of Physical Chemistry Letters, 2024, 15: 1321−1327.

[11] HUANG Meng, HE Qiu, WANG Jun-jun, LIU Xiong, XIONG Fang-yu, LIU Yu, GUO Rui-ting, ZHAO Yan, YANG Jin-long, MAI Li-qiang. NH_4^+ deprotonation at interfaces induced reversible H_3O^+/NH_4^+ co-insertion/extraction [J]. Angewandte Chemie International Edition, 2023, 62: e202218922.

[12] JIANG Ming-wei, HOU Zhi-dong, REN Ling-bo, ZHANG Yu, WANG Jian-gan. Prussian blue and its analogues for aqueous energy storage: From fundamentals to advanced

devices [J]. Energy Storage Materials, 2022, 50: 618−640.
[13] XING Jun-jie, FU Xiu-li, GUAN Shun-dong, ZHANG Yu, LEI Ming, PENG Zhi-jian. Novel K−V−Fe Prussian blue analogues nanocubes for high-performance aqueous ammonium ion batteries [J]. Applied Surface Science, 2021, 543: 148843.
[14] BOMMIREDDY P R, KARNAM J B, CHANDRA S M, PARK S H. Ni−Co PBA-decorated CNTs as battery-type cathode materials for potassium-ion hybrid capacitors [J]. Journal of Energy Storage, 2023, 62: 106870.
[15] SHEN Yuan-hao, ZOU Juan, LAN Hai-hui, DING Yi-ran, LIANG Zi-jia, YANG Zhong-zhuo, ZENG Zi-yue, LONG Jun-cai, ZHAO Yuan-xin, FU Lei, ZENG Meng-qi. Unlocking Prussian blue analogues inert-site to achieve high-capacity ammonium storage [J]. Advanced Functional Materials, 2024, 34: 2400598.
[16] WU Han, HAO Jun-nan, JIANG Yun-ling, JIAO Yi-ran, LIU Jia-hao, XU Xin, DAVEY K, WANG Chun-sheng, QIAO Shi-zhang. Alkaline-based aqueous sodium-ion batteries for large-scale energy storage [J]. Nature Communications, 2024, 15: 575.
[17] LI Ren-jie, YU Jing-ya, CHEN Fei-yang, SU Ya-qiong, CHAN Kang, XU Zheng-long. High-power and ultrastable aqueous calcium-ion batteries enabled by small organic molecular crystal anodes [J]. Advanced Functional Materials, 2023, 33: 2214304.
[18] WANG Tong-kai, LI Xiao-juan, ZHAO Shun-shun, BU Hong-xia, LI Chuan-lin, LI Na, ZHANG Xi-xi, XU Xi-jin. Rocking-chair ammonium ion battery with high rate and long-cycle life [J]. Chinese Chemical Letters, 2024, 35: 108449.
[19] LIN Yu-tong, HAN Bing, ZHANG Dong-lan, LIU Xue-ya, WANG Zi-li, WANG Zheng-yu, SI Liang, ZHANG Sen, DENG Chao. Low-strain binary hexacyanoferrate nanocuboids with concentration-gradient structure towards fast and durable energy storage [J]. Journal of Energy Chemistry, 2022, 74: 72−84.
[20] ZHENG Run-tian, LI Yu-hang, YU Hao-xiang, ZHANG Xi-kun, YANG Ding, YAN Lei, LI Yu, SHU Jie, SU Bao-lian. Ammonium ion batteries: Material, electrochemistry and strategy [J]. Angewandte Chemie International Edition, 2023, 62: e202301629.
[21] ZHANG Xi-kun, XIA Mao-ting, YU Hao-xiang, ZHANG Jun-wei, YANG Zheng-wei, ZHANG Li-yuan, SHU Jie. Hydrogen bond-assisted ultra-stable and fast aqueous NH_4^+ storage [J]. Nano-Micro Letters, 2021, 13: 139.
[22] YANG Wen-hui, ZHANG Xi-kun, SHU Guang-chang, YU Hao-xiang, ZHANG Li-yuan, YAN Lei, SHU Jie. An aqueous rechargeable copper ammonium hybrid battery with good cycling performance [J]. Inorganic Chemistry Frontiers, 2024, 11: 1450−1457.
[23] FAN Lei-yu, SHU Guang-chang, LIU Yi-wen, YU Hao-xiang, YAN Lei, ZHANG Li-yuan, SHU Jie. Cu-substituted nickel hexacyanoferrate with tunable reaction potentials for superior ammonium ion storage [J]. Journal of Materials Science & Technology, 2024, 169: 19−27.
[24] CHEN Lu, SUN Wen-lu, XU Kui, DONG Qing-yu, ZHENG Lei, WANG Jun, LU De-rong, SHEN Yan-bin, ZHANG Jun-yu, FU Fang, KONG Hua-bin, QIN Jia-qian, CHEN Hong-wei. How Prussian blue analogues can be stable in concentrated aqueous electrolytes [J]. ACS Energy Letters, 2022, 7: 1672−1678.
[25] HENG Yong-li, GU Zhen-yi, GUO Jin-zhi, WU Xing-long. Research progresses on vanadium-based cathode materials for aqueous zinc-ion batteries [J]. Acta Physico Chimica Sinica, 2020, 37: 2005013−2005010.
[26] WANG Dong-hong, LV Hai-ming, HUSSAIN T, YANG Qi, LIANG Guo-jin, ZHAO Yu-wei, MA Long-tao, LI Qing, LI Hong-fei, DONG Bin-bin, KAEWMARAYA T, ZHI Chun-yi. A manganese hexacyanoferrate framework with enlarged ion tunnels and two-species redox reaction for aqueous Al-ion batteries [J]. Nano Energy, 2021, 84: 105945.
[27] YANG Jun, HOU Wen-xiu, YE Ling-qian, HOU Guo-yu, YAN Chao, ZHANG Yu. Vanadium hexacyanoferrate Prussian blue analogs for aqueous proton storage: Excellent electrochemical properties and mechanism insights [J]. Small, 2023, 20: e2305386.
[28] QIU Shen, XU Yun-kai, WU Xian-yong, JI Xiu-lei. Prussian blue analogues as electrodes for aqueous monovalent ion batteries [J]. Electrochemical Energy Reviews, 2022, 5: 242−262.
[29] ELLIS D, ECKHOFF M, NEFF V D. Electrochromism in the mixed-valence hexacyanides. 1: Voltammetric and spectral studies of the oxidation and reduction of thin films of Prussian blue [J]. The Journal of Physical Chemistry, 1981, 85: 1225−1231.
[30] ITAYA K, ATAKA T, TOSHIMA S. Electrochemical preparation of a Prussian blue analog: Iron−ruthenium cyanide [J]. Journal of the American Chemical Society, 1982, 104: 3751−3752.
[31] TSIAFOULIS C G, TRIKALITIS P N, PRODROMIDIS M I. Synthesis, characterization and performance of vanadium hexacyanoferrate as electrocatalyst of H_2O_2 [J]. Electrochemistry Communications, 2005, 7: 1398−1404.
[32] ZHANG Yan-jun, WANG Yao, LU Liang, SUN Chun-wen, DENIS Y W. Vanadium hexacyanoferrate with two redox active sites as cathode material for aqueous Zn-ion batteries [J]. Journal of Power Sources, 2021, 484: 229263.
[33] HOU Wen-xiu, YAN Chao, SHAO Pan-run, DAI Kun, YANG Jun. Interface and electronic structure engineering induced Prussian blue analogues with ultra-stable capability for aqueous NH_4^+ storage [J]. Nanoscale, 2022, 14: 8501−8509.
[34] ZHANG Jian, CUI Ren-jie, GAO Chen-cheng, BIAN Lin-yi, PU Yong, ZHU Xin-bao, LI Xing-ao, HUANG Wei. Cation-modulated HER and OER activities of hierarchical VOOH hollow architectures for high-efficiency and stable overall water splitting [J]. Small, 2019, 15: e1904688.
[35] DU Guang-yuan, TAO Meng-li, LI Jie, YANG Ting-ting, GAO Wei, DENG Jian-hua, QI Yu-ruo, BAO Shu-juan, XU Mao-wen. Low-operating temperature, high-rate and durable solid-state sodium-ion battery based on polymer electrolyte and Prussian blue cathode [J]. Advanced Energy Materials, 2020, 10: 1903351.
[36] BASTER D, KONDRACKI Ł, OVEISI E, TRABESINGER S, GIRAULT H H. Prussian blue analogue−sodium−vanadium hexacyanoferrate as a cathode material for Na-ion batteries [J]. ACS Applied Energy Materials, 2021, 4: 9758−9765.
[37] SOOKHAKIAN M, BASIRUN W J, TERIDI M A M, MAHMOUDIAN M R, AZARANG M, ZALNEZHAD E, YOON G H, ALIAS Y. Prussian blue-nitrogen-doped graphene nanocomposite as hybrid electrode for energy storage applications [J]. Electrochimica Acta, 2017, 230: 316−323.
[38] YANG Jun, HOU Wen-xiu, PAN Run, ZHOU Mu, ZHANG Shuo-zhou, ZHANG Yu. The interfacial electronic engineering in polyhedral MOF derived Co-doped $NiSe_2$

composite for upgrading rate and longevity performance of aqueous energy storage [J]. Journal of Alloys and Compounds, 2022, 897: 163187.
[39] ZHANG Xi-kun, XIA Mao-ting, LIU Ting-ting, PENG Na, YU Hao-xiang, ZHENG Run-tian, ZHANG Li-yuan, SHUI Miao, SHU Jie. Copper hexacyanoferrate as ultra-high rate host for aqueous ammonium ion storage [J]. Chemical Engineering Journal, 2021, 421: 127767.
[40] LEE J H, ALI G, KIM D H, CHUNG K Y. Metal-organic framework cathodes based on a vanadium hexacyanoferrate prussian blue analogue for high-performance aqueous rechargeable batteries [J]. Advanced Energy Materials, 2016, 7: 1601491.
[41] JIANG Ping, LEI Zhen-yu, CHEN Liang, SHAO Xue-cheng, LIANG Xin-miao, ZHANG Jun, WANG Yan-chao, ZHANG Jiu-jun, LIU Zhao-ping, FENG Ji-wen. Polyethylene glycol-Na^+ interface of vanadium hexacyanoferrate cathode for highly stable rechargeable aqueous sodium-ion battery [J]. ACS Applied Materials & Interfaces, 2019, 11: 28762−28768.
[42] SHAO Yuan-long, EL-KADY M F, SUN Jing-yu, LI Yao-gang, ZHANG Qing-hong, ZHU Mei-fang, WANG Hong-zhi, DUNN B, KANER R B. Design and mechanisms of asymmetric supercapacitors [J]. Chemical Reviews, 2018, 118: 9233−9280.
[43] WEI Ting-ting, PENG Pan-pan, JI Yu-rui, ZHU Yan-rong, YI Ting-feng, XIE Ying. Rational construction and decoration of $Li_5Cr_7Ti_6O_{25}$@C nanofibers as stable lithium storage materials [J]. Journal of Energy Chemistry, 2022, 71: 400−410.
[44] REN Wen-hao, CHEN Xian-jue, ZHAO Chuan. Ultrafast aqueous potassium-ion batteries cathode for stable intermittent grid-scale energy storage [J]. Advanced Energy Materials, 2018, 8: 1801413.
[45] ZHANG Ru-ding, WANG Shun, CHOU Shu-lei, JIN Hui-le. Research development on aqueous ammonium-ion batteries [J]. Advanced Functional Materials, 2022, 32: 2112179.
[46] WESSELLS C D, HUGGINS R A, CUI Y. Copper hexacyanoferrate battery electrodes with long cycle life and high power [J]. Nature Communications, 2011, 2: 550.
[47] WU Xian-yong, QI Yi-tong, HONG J J, LI Zhi-fei, HERNANDEZ A S, JI Xiu-lei. Rocking-chair ammonium-ion battery: A highly reversible aqueous energy storage system [J]. Angewandte Chemie International Edition, 2017, 56: 13026−13030.
[48] CHEN Liang, SHAO He-zhu, ZHOU Xu-feng, LIU Guo-qiang, JIANG Jun, LIU Zhao-ping. Water-mediated cation intercalation of open-framework indium hexacyanoferrate with high voltage and fast kinetics [J]. Nature Communications, 2016, 7: 11982.
[49] LIANG Peng-hua, XU Teng-fei, ZHU Kong-jun, RAO Yu, ZHENG Hong-juan, WU Meng, CHEN Jia-tao, LIU Jin-song, YAN Kang, WANG Jing, ZHANG Rui-feng. Heterogeneous interface-boosted zinc storage of $H_2V_3O_8$ nanowire/$Ti_3C_2T_x$ MXene composite toward high-rate and long cycle lifespan aqueous zinc-ion batteries [J]. Energy Storage Materials, 2022, 50: 63−74.
[50] DU Ling-yu, BI Song-shan, YANG Min, TIE Zhi-wei, ZHANG Min-hui, NIU Zhi-qiang. Coupling dual metal active sites and low-solvation architecture toward high-performance aqueous ammonium-ion batteries [J]. Proceedings of the National Academy of Sciences of the United States of America, 2022, 119: e2214545119.
[51] LI Si-yun, XIA Mao-ting, XIAO Cheng-xiang, ZHANG Xi-kun, YU Hao-xiang, ZHANG Li-yuan, SHU Jie. Common ion effect enhanced Prussian blue analogues for aqueous ammonium ion storage [J]. Dalton Transactions, 2021, 50: 6520−6527.

用于水系铵离子电池正极材料的钒基普鲁士蓝类似物的制备、电化学性能及储能机理

李桃桃[1]，曲津朋[1]，赵路路[1]，王鹏飞[1]，张军红[2]，伊廷锋[1,3]

1. 东北大学 材料科学与工程学院，沈阳 110819；
2. 聊城大学 化学化工学院 山东省化学储能与新型电池技术重点实验室，聊城 252059；
3. 东北大学秦皇岛分校 资源与材料学院 河北省电介质与电解质功能材料重点实验室，秦皇岛 066004

摘 要：为了探索用于水系铵离子电池(AAIBs)的高性能正极材料，采用水热共沉淀法制备钒基普鲁士蓝类似物复合材料(VFe-PBAs)，旨在提高 NH_4^+的可逆存储能力。得益于其稳定的三维结构和宽敞的间隙位置，VFe-PBAs-2 正极表现出极优的电化学活性和倍率性能，在 1000 mA/g 的电流密度下达到了 84.3 mA·h/g 的高比容量。此外，VFe-PBAs-2 正极表现出极佳的长期循环稳定性，在 5000 mA/g 的条件下，经过 3×10^4 次循环后，容量保持率依然高达 85.2%。所合成的正极材料结合了钒离子的高电化学活性，显著促进了 NH_4^+的快速传输。此外，通过电化学动力学测试和先进的非原位表征手段揭示了 NH_4^+在 VFe-PBAs-2 正极材料中的嵌入/脱出机理。实验结果表明，钒改性的 VFe-PBA-2 正极材料能显著提升铵离子电池的容量、电化学活性以及循环稳定性，从而实现高性能的铵离子存储。

关键词：能量储存；水系铵离子电池；普鲁士蓝类似物；倍率性能；循环稳定性

(Edited by Wei-ping CHEN)